HEALTH AND MEDICINE

Integrated cascade nanozyme catalyzes in vivo ROS scavenging for anti-inflammatory therapy

Yufeng Liu[1]*, Yuan Cheng[1]*, He Zhang[2], Min Zhou[1], Yijun Yu[3], Shichao Lin[1], Bo Jiang[4], Xiaozhi Zhao[4], Leiying Miao[3], Chuan-Wan Wei[5], Quanyi Liu[6], Ying-Wu Lin[5], Yan Du[6], Christopher J. Butch[1†], Hui Wei[1,7,8†]

Here, an integrated cascade nanozyme with a formulation of Pt@PCN222-Mn is developed to eliminate excessive reactive oxygen species (ROS). This nanozyme mimics superoxide dismutase by incorporation of a Mn–[5,10,15,20-tetrakis(4-carboxyphenyl)porphyrinato]–based metal-organic framework compound capable of transforming oxygen radicals to hydrogen peroxide. The second mimicked functionality is that of catalase by incorporation of Pt nanoparticles, which catalyze hydrogen peroxide disproportionation to water and oxygen. Both in vitro and in vivo experimental measurements reveal the synergistic ROS-scavenging capacity of such an integrated cascade nanozyme. Two forms of inflammatory bowel disease (IBD; i.e., ulcerative colitis and Crohn's disease) can be effectively relieved by treatment with the cascade nanozyme. This study not only provides a new method for constructing enzyme-like cascade systems but also illustrates their efficient therapeutic promise in the treatment of in vivo IBDs.

INTRODUCTION

Cascade catalytic reaction systems in living organisms have evolved by confining multiple enzymes within subcellular compartments to ensure accurate signal transduction and effective metabolism (1). Confined cascade reactions gain advantage over conventional multistep reactions by reducing diffusion barriers, enhancing local concentrations of intermediates, and improving atom economy of overall reactions (2). Inspired by the advantages of these systems, substantial efforts have been made to organize enzymes on different scaffolds to mimic these efficient cascade systems (3–6). However, because of the high cost, low stability, and potential immunogenicity of scaffold-supported enzyme cascades, the design and utility of natural enzyme–based cascade reactions in biomedical applications (especially in vivo therapeutics) are limited.

To tackle these limitations, enzyme mimics have been exploited to construct cascade reactions. Among these, nanozymes, enzyme-like nanomaterials, have received particular interest due to low cost, high stability, multifunctionality, and ease of large-scale production (7–20). Numerous efforts have explored the combination of nanozymes with natural enzymes to mimic cascade reactions (21–23), with one example being the combination of glucose oxidase and a peroxidase mimic for the selective detection of glucose (21). However,

very few nanozyme-only cascade reaction systems have been reported, and most exhibit only moderate activity while requiring mutually incompatible reaction conditions (such as different reaction pH), which limit the in vivo applications (24–27). For example, Au nanoparticles (NPs) with both glucose oxidase–like and peroxidase-like activities were used to first convert glucose to hydrogen peroxide (phosphate buffer, pH 9) and then to oxidize a substrate with hydrogen peroxide to generate a colored product for biosensing (acetate buffer, pH 4.5) (26). Here, we report a single-component nanozyme-based cascade reaction system with high overall activity and demonstrate that such a nanozyme can be effectively used for in vivo therapy of inflammatory bowel diseases (IBDs) associated with excess reactive oxygen species (ROS).

Numerous inflammatory diseases, including hepatitis, glomerulonephritis, and IBD, are associated with excess ROS production (28). Anti-ROS therapy for these diseases is typically achieved using stoichiometric antioxidants, which are consumed as they deplete ROS (29). In contrast, cellular anti-ROS pathways use ROS-scavenging enzymes, including superoxide dismutase (SOD) and catalase (CAT). Unlike therapeutic antioxidants, these enzymes are conserved as they catalyze the anti-ROS cascade reactions, beginning with the dismutation of $^\bullet O_2^-$ into H_2O_2 by SOD and, subsequently, the conversion of H_2O_2 to water and O_2 by CAT. SOD (usually in mitochondria or cytosol) and CAT (usually in peroxisome) are not in the same subcellular compartment, meaning that an additional transport step is needed between the generation and degradation of H_2O_2, and raising the possibility that a cascade nanozyme may be able to surpass the efficiency of the native system (30, 31). While use of SOD/CAT for catalytic ROS-scavenging therapy would be desired, the low stability and high cost of these enzymes, along with the potential for immune response, make this approach challenging. Instead, we envisioned that the development of cascade nanozymes would be an effective strategy to mimic the reactions for anti-ROS therapy. Although several nanozymes with multiple ROS-scavenging abilities have been applied in in vivo therapies (32–34), most of them suffer from the limitations of single active site, low specific surface areas, and moderate biocompatibility. We reasoned that using biocompatible metal-organic frameworks (MOFs) can tackle these challenges due to their excellent performance in biomedical applications and flexibility of design and synthesis.

[1]Department of Biomedical Engineering, College of Engineering and Applied Sciences, Nanjing University, Nanjing, Jiangsu 210093, China. [2]Department of Periodontology, Nanjing Stomatological Hospital, Medical School of Nanjing University, Nanjing, Jiangsu 210093, China. [3]Department of Cariology and Endodontics, Nanjing Stomatological Hospital, Medical School of Nanjing University, Nanjing, Jiangsu 210093, China. [4]Department of Urology, Drum Tower Hospital, Medical School of Nanjing University, Institute of Urology, Nanjing University, Nanjing, Jiangsu 210008 China. [5]Laboratory of Protein Structure and Function, School of Chemistry and Chemical Engineering, University of South China, Hengyang, Hunan 421001, China. [6]State Key Laboratory of Electroanalytical Chemistry, Changchun Institute of Applied Chemistry, Chinese Academy of Science, Changchun, Jilin 130022, China. [7]Nanjing National Laboratory of Microstructures, Jiangsu Key Laboratory of Artificial Functional Materials, Nanjing University, Nanjing, Jiangsu 210093, China. [8]State Key Laboratory of Analytical Chemistry for Life Science and State Key Laboratory of Coordination Chemistry, School of Chemistry and Chemical Engineering, Chemistry and Biomedicine Innovation Center (ChemBIC), Nanjing University, Nanjing, Jiangsu 210023, China.
*These authors contributed equally to this work.
†Corresponding author. Email: weihui@nju.edu.cn (H.W.); chrisbutch@gmail.com (C.J.B.)

To demonstrate our hypothesis, here, we designed and synthesized an integrated SOD/CAT mimetic cascade nanozyme (designated as Pt@PCN222-Mn) by introducing an SOD-like moiety of Mn(III) porphyrin and a CAT-like Pt NP within a nanoscale Zr-based MOF, PCN222 (Fig. 1). Compared with the combination of PCN222 with Mn(III) porphyrin (PCN222-Mn) and Pt NPs, the integrated cascade nanozyme Pt@PCN222-Mn exhibited higher efficiency in both SOD- and CAT-like activities in vitro. Furthermore, the cascade nanozyme also showed synergistically enhanced ROS-scavenging activity in vivo and effectively protected mice from ROS-related IBD, a still incurable chronic disease. These results not only demonstrated the excellent ROS-scavenging capacity of integrated cascade nanozymes but also broadened the potential in vivo biomedical applications of designed cascade nanozymes.

RESULTS

Design, synthesis, and characterization of Pt@PCN222-Mn

The Pt@PCN222-Mn cascade nanozymes with both SOD- and CAT-like activities were designed and synthesized, as shown in Fig. 2A. First, the manganese porphyrin [5,10,15,20-tetrakis(4-carboxyphenyl)-porphyrinato]–Mn(III) chloride (TCPP-Mn), an analog of the mononuclear Mn(III) active site in Mn SOD, was synthesized to mimic SOD (scheme S1). The successful synthesis of TCPP-Mn was confirmed by nuclear magnetic resonance (NMR), Fourier transform infrared (FTIR) spectrometry, and ultraviolet (UV)–visible spectroscopic measurements (figs. S1 to S3).

Then, the TCPP-Mn containing nanoscale MOF, named as PCN222-Mn, was synthesized. The formation of PCN222-Mn was confirmed by transmission electron microscopic (TEM) and scanning electron microscopic (SEM) imaging. As shown in Fig. 2 (B and C) and figs. S4 and S5, PCN222-Mn exhibited uniform lenticular morphology with an average size of 200 nm. The powder x-ray diffraction (PXRD) pattern of PCN222-Mn in Fig. 2D was consistent with a previous report (35). PCN222-Mn exhibited absorption peaks of 470, 570, and 610 nm, demonstrating the successful incorporation of TCPP-Mn. A slight red shift of PCN222-Mn was also observed because of the increased particle size (fig. S3). Figure S6 showed that the zeta potential of PCN222-Mn was about +32 mV, indicating excellent dispersibility in aqueous solution and potential for further in vivo applications without agglomeration concerns.

Last, the Pt@PCN222-Mn cascade nanozymes were fabricated by incorporating polyvinylpyrrolidone (PVP)–stabilized Pt NPs within PCN222-Mn, using a previous synthetic methodology (36). The PVP-stabilized Pt NPs with a size of less than 5 nm were synthesized and characterized by TEM imaging and PXRD measurement (figs. S7 and S8). Three cascade nanozymes with 0.7, 2.2, and 6 weight % (wt %) of Pt NPs were synthesized (Fig. 2A) and termed as Pt@PCN222-Mn-1, Pt@PCN222-Mn-3, and Pt@PCN222-Mn-5, respectively. PXRD patterns showed that all the three cascade nanozymes had similar peaks to PCN222-Mn, indicating the intact crystallinity of PCN222-Mn after Pt NP encapsulation (Fig. 2D). Because of the ultrasmall size and low content of Pt NPs, the corresponding peaks of Pt NPs were not obvious in the PXRD patterns. TEM images showed that all three cascade nanozymes maintained uniform lenticular morphology with an average size of 200 nm. Moreover, the gradually increased Pt NP contents within the MOF scaffold from Pt@PCN222-Mn-1 to Pt@PCN222-Mn-5 were observed (Fig. 2, E to G, and fig. S9). A typical high-resolution TEM image of Pt@PCN222-Mn-5 showed a lattice spacing of 0.224 nm, which further confirmed the successful encapsulation of Pt NPs (Fig. 2H). SEM
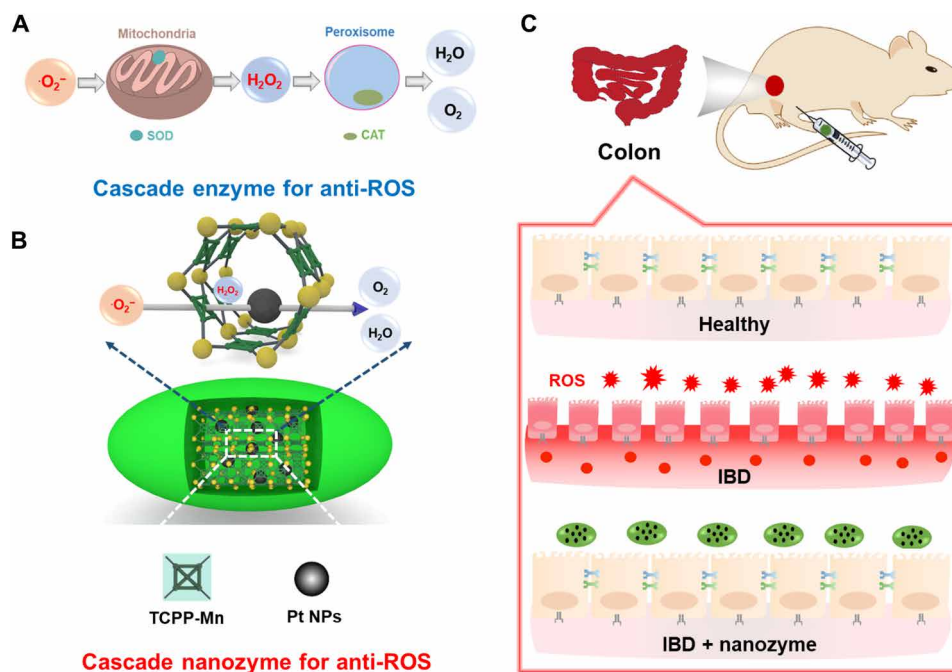

Fig. 1. Schematic illustration of the design of an integrated nanozyme with cascade anti-ROS activity for IBD therapy. (**A**) Cellular cascade enzymes for anti-ROS. The therapeutic efficacy of such a system is limited because of the different subcellular locations of SOD and CAT enzymes and limited extracellular stability. (**B**) Constructing a cascade nanozyme for anti-ROS therapy by embedding Pt NPs inside PCN222-Mn MOF. Nanoscale proximity of catalytic active sites promotes the cascade reactions. (**C**) The IBD of mice can be effectively relieved through treatment with the integrated cascade nanozyme.
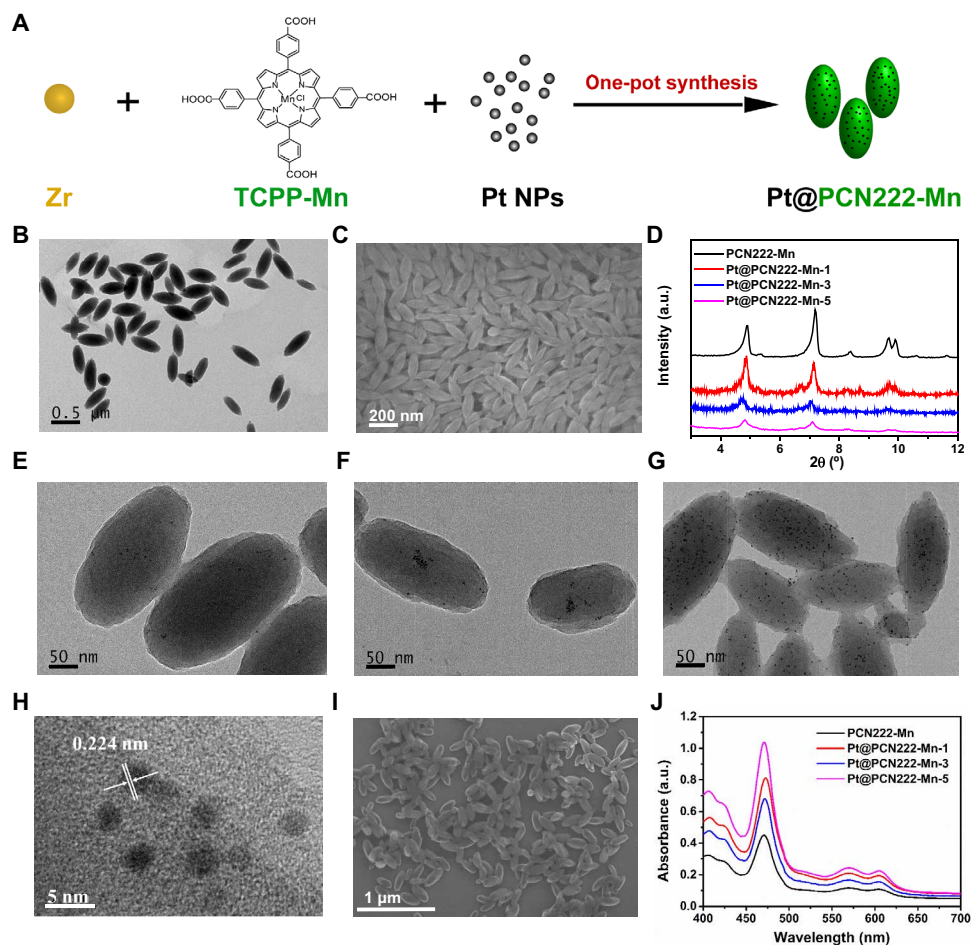
Fig. 2. Synthesis and structural characterization of Pt@PCN222-Mn and related materials. (**A**) Synthesis procedure of Pt@PCN222-Mn. (**B**) Transmission electron microscopic (TEM) and (**C**) Scanning electron microscopic (SEM) images of PCN222-Mn. (**D**) Powder x-ray diffraction (PXRD) patterns of PCN222-Mn, Pt@PCN222-Mn-1, Pt@PCN222-Mn-3, and Pt@PCN222-Mn-5. TEM images of (**E**) Pt@PCN222-Mn-1, (**F**) Pt@PCN222-Mn-3, and (**G**) Pt@PCN222-Mn-5. (**H**) High-resolution TEM and (**I**) SEM images of Pt@PCN222-Mn-5. (**J**) Absorption spectra of PCN222-Mn, Pt@PCN222-Mn-1, Pt@PCN222-Mn-3, and Pt@PCN222-Mn-5. a.u., arbitrary units.

images also demonstrated similar a morphology between PCN222-Mn and Pt@PCN222-Mn-5 (Fig. 2, C and I). UV-visible spectroscopy measurement confirmed the presence of TCPP-Mn within the three nanozymes (Fig. 2J). The zeta potentials of Pt@PCN222-Mn-1, Pt@PCN222-Mn-3, and Pt@PCN222-Mn-5 were about 30, 32, and 26 mV, respectively, which endowed them with excellent dispersibility in aqueous solution for further in vivo applications (fig. S10). Nitrogen adsorption isotherms of PCN222-Mn and Pt@PCN222-Mn-5 were measured, and the corresponding data showed their higher Brunauer-Emmett-Teller (BET) surface areas than other anti-ROS nanozymes (fig. S11 and table S1).

In vitro SOD-like activity of the cascade nanozymes
Since scavenging $^{\bullet}O_2^-$ is the initial step of the anti-ROS cascade reaction, the SOD-like activities of TCPP, TCPP-Mn, and PCN222-Mn were first investigated by monitoring their capability to eliminate $^{\bullet}O_2^-$, generated from a mixture of xanthine (X) and xanthine oxidase (XO). As shown in fig. S12 (A and B), the metal-free porphyrin TCPP had no SOD-like activity, whereas both TCPP-Mn and PCN222-Mn had strong SOD-like activities, indicating the key role of Mn in porphyrin for mimicking SOD-like activity. The slightly higher SOD-like activity of PCN222-Mn was probably due to its

better aqueous dispersity than TCPP-Mn, as the latter often suffers from poor water solubility.

The SOD-like activities of PCN222-Mn, Pt@PCN222-Mn-1, Pt@PCN222-Mn-3, and Pt@PCN222-Mn-5 were then systematically evaluated by using nitrotetrazolium blue chloride (NBT) as a sensitive $^{\bullet}O_2^-$ indicator. NBT is specifically reduced by $^{\bullet}O_2^-$ to produce an absorbance at 550 nm. As shown in fig. S13 (A to D), kinetic curves produced by continuously monitoring the changes of absorbance at 550 nm showed a positive correlation between the SOD-like activities and the concentrations of nanozymes. At the same concentration, Pt@PCN222-Mn-5 showed the highest SOD-like activity among the enzyme mimics (Fig. 3A). Pt NPs showed that the concentration-dependent SOD-like activity and the $^{\bullet}O_2^-$ elimination ability increased with the increase of Pt contents in Pt@PCN222-Mn nanozymes (Fig. 3B). Moreover, electron paramagnetic resonance (EPR) spectroscopy was used to evaluate the SOD-like activity of these nanozymes, and the results further demonstrated the highest SOD-like activity of Pt@PCN222-Mn-5 (fig. S14).

In vitro CAT-like activity of the cascade nanozymes
H_2O_2, the downstream product of $^{\bullet}O_2^-$ dismutation, like $^{\bullet}O_2^-$ can also be a potent oxidant. In vivo, CAT catalyzes the decomposition
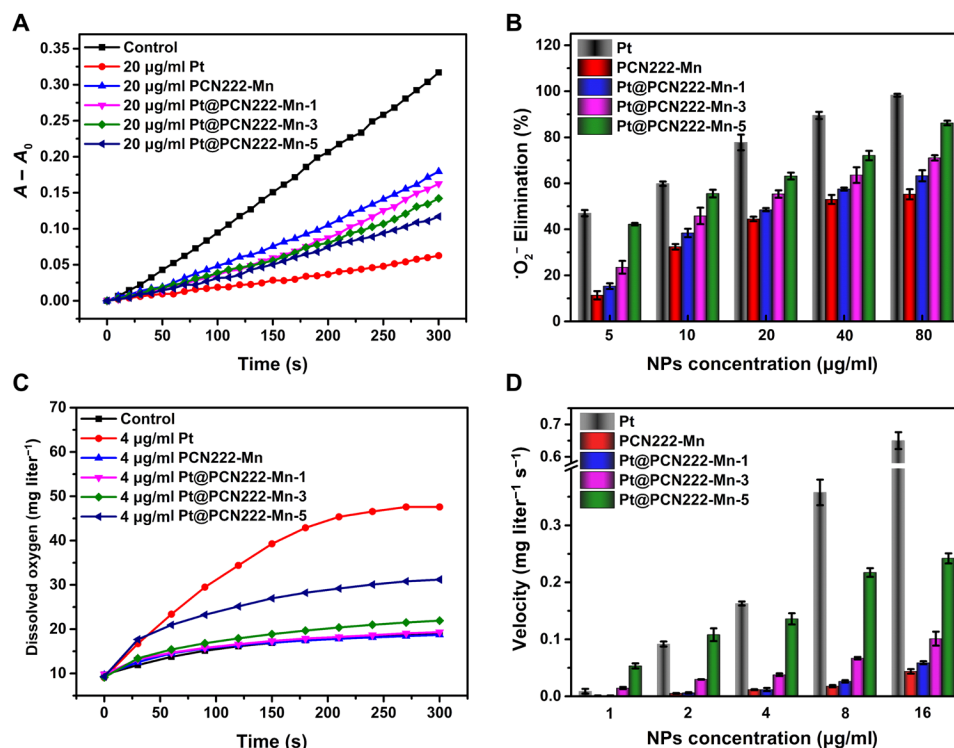
Fig. 3. ROS-scavenging activities of Pt@PCN222-Mn and related materials. (**A**) Typical kinetic curves of $A - A_0$ (550 nm) for monitoring the reduction of NBT with X and XO in the absence and presence of Pt, PCN222-Mn, Pt@PCN222-Mn-1, Pt@PCN222-Mn-3, and Pt@PCN222-Mn-5. (**B**) Dependence between the elimination efficiency of $^{\bullet}O_2^-$ and concentrations of nanozymes. (**C**) Typical kinetic curves of oxygen generation from the decomposition of H_2O_2 (50 mM) in the presence of Pt, PCN222-Mn, Pt@ PCN222-Mn-1, Pt@PCN222-Mn-3, and Pt@PCN222-Mn-5. (**D**) Dependence between the oxygen-production velocities in the first 60 s and concentrations of nanozymes. The data are shown as means ± SD ($n = 3$).

of H_2O_2 into H_2O and O_2, in the second crucial step of the ROS-scavenging cascade system. By monitoring the generated O_2 from decomposition of H_2O_2, the CAT-like activities of these nanozymes were then evaluated. Figure S13 (E to H) showed the O_2 generation rates from different H_2O_2 concentrations in the absence and presence of PCN222-Mn, Pt@PCN222-Mn-1, Pt@PCN222-Mn-3, and Pt@PCN222-Mn-5. At the same concentration, Pt@PCN222-Mn-5 also showed the highest CAT-like activity among other MOF-based enzyme mimics (Fig. 3C). The oxygen-generation velocities of first 60 s were shown in Fig. 3D, indicating a positive correlation of Pt NP contents and CAT-like activities. Note that the CAT-like activity of Pt NPs showed a stronger concentration dependence than SOD-like activity. PCN222-Mn also had a basal level of CAT-like activity. By further analyzing the data in fig. S13, it could be concluded that the SOD-like activity was mainly from the TCPP-Mn moiety, whereas the CAT-like activity was mainly from Pt NPs.

Synergistic effects of Pt@PCN222-Mn-5

To investigate the potential synergistic effects of the cascade nanozyme Pt@PCN222-Mn-5, its SOD- and CAT-like activities were compared with free Pt NPs and Pt NPs physically mixed with PCN222-Mn. Figure 4 (A and B) showed that Pt@PCN222-Mn-5 had the highest SOD- and CAT-like activities, demonstrating a synergistic effect. We also noted that the synergistic effect was more pronounced for CAT-like activities. This was reasonable for the following reasons. First, the synergistically enhanced activities of Pt@PCN222-Mn could be attributed to their pore confinement effect, which not only loaded

high dense of active Pt NPs but also avoided the aggregation of small-sized active Pt NPs. Second, while both SOD- and CAT-like activities of Pt NPs were concentration dependent, the CAT-like activity exhibited a stronger concentration dependence (Fig. 3). It indicated that Pt NPs with low concentration had weaker CAT-like activity. Combined with the concentration-dependent activities and pore confinement effect, the synergistic effects of SOD- and CAT-like activities were reasonably different in Pt@PCN222-Mn (37).

Further kinetic analysis of SOD/CAT cascade reaction suggests that diffusion of H_2O_2 is rate limiting in the overall reaction likely due to the generated H_2O_2 interacting with the Mn nucleus, thus occupying the active site and blocking the interaction with a new $^{\bullet}O_2^-$ molecule; synergy thus arises as the diffusion process is greatly accelerated by nanoconfinement of the Pt NP near the Mn nuclei (fig. S15). Pt@PCN222-Mn-5 consequently showed the best performance in both SOD- and CAT-like activities and was used as the cascade nanozyme for the subsequent study.

Cellular evaluation of Pt@PCN222-Mn-5

The cytotoxicity of Pt@PCN222-Mn-5 was evaluated by using CT26 cell line as a model (PCN222-Mn was also studied as a comparison to isolate any effects related to Pt NPs). Cell Counting Kit-8 (CCK-8) assays showed that both Pt@PCN222-Mn-5 and PCN222-Mn exhibited no obvious cytotoxicity below a concentration of 80 μg/ml while showing a slight cytotoxicity above 100 μg/ml (fig. S16). Para-quat (PQ) was then applied to the cells treated at 0.1, 0.5, and 1 μg/ml to stimulate the overproduction of intracellular ROS levels. As

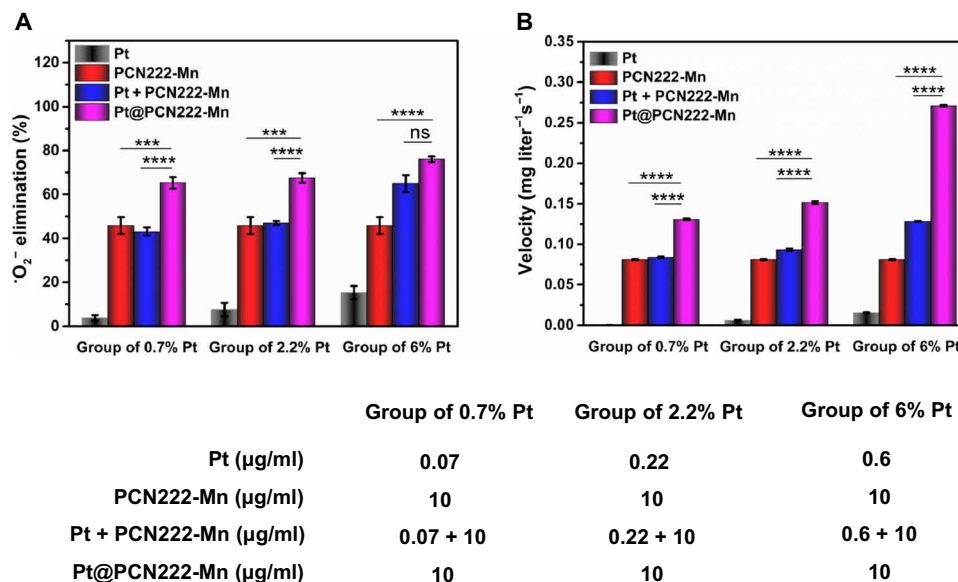|	Group of 0.7% Pt	Group of 2.2% Pt	Group of 6% Pt
Pt (µg/ml)	0.07	0.22	0.6
PCN222-Mn (µg/ml)	10	10	10
Pt + PCN222-Mn (µg/ml)	0.07 + 10	0.22 + 10	0.6 + 10
Pt@PCN222-Mn (µg/ml)	10	10	10

Fig. 4. Synergistic ROS-scavenging activity of Pt@PCN222-Mn-5. (**A**) Elimination efficiency of $\cdot O_2^-$ with different concentrations of Pt, PCN222-Mn, Pt + PCN222-Mn, and Pt@PCN222-Mn. (**B**) Oxygen-production velocities in the first 60 s, with different concentrations of Pt, PCN222-Mn, Pt + PCN222-Mn, and Pt@PCN222-Mn. The data are shown as means ± SD ($n = 3$). ***$P < 0.005$ and ****$P < 0.001$; ns, not significant; t test.

shown in fig. S17, the PQ-treated group showed the highest fluorescence, demonstrating the overproduced ROS levels. The fluorescence of Pt@PCN222-Mn-5– and PCN222-Mn–pretreated groups were reduced at all concentrations, thus demonstrating the excellent ROS-scavenging ability of both Pt@PCN222-Mn-5 and PCN222-Mn.

In vivo anti-inflammation therapy

On the basis of the excellent ROS-scavenging activity and good biocompatibility of Pt@PCN222-Mn-5, its in vivo therapeutic efficacy was then investigated for the treatment of ulcerative colitis (UC) and Crohn's disease (CD) in murine models of the disease states.

UC is a typical IBD, which is often accompanied with overproduced ROS (*38*). The therapeutic efficacy of Pt@PCN222-Mn-5 toward UC was first evaluated together with 5-aminosalicylic acid (5-ASA), a medication for IBD treatment, as a positive control. Figure S18A summarizes the overall experimental procedure. Mice were fed with dextran sulfate sodium (DSS) (2 wt % in water) for five consecutive days (days 1 to 5) to induce UC. Successful onset of UC was indicated by body weight loss on day 5 for all DSS-induced groups (fig. S18B). After that, PCN222-Mn, Pt@PCN222-Mn-5, and 5-ASA were administered as treatment by intraperitoneal injection to each mouse on three consecutive days (days 6, 7, and 8). As shown in fig. S18 (C and G), colon lengths and hematoxylin and eosin (H&E)–stained colon sections indicated that the treatment of nanozymes (1.0 mg/kg) had therapeutic effectiveness similar to 5-ASA (1.0 mg/kg). Furthermore, levels of inflammatory cytokines tumor necrosis factor–α (TNF-α) and interleukin-1β (IL-1β) [measured by immunohistochemical (IHC) staining] showed that the nanozyme-treated groups had lower cytokine levels than 5-ASA–treated mice (figs. S18, D and F, and S19). Combined, these results indicate that Pt@PCN222-Mn-5 successfully relieved the UC disease state.

To optimize the dosing of cascade nanozyme Pt@PCN222-Mn-5 and further investigate the synergistic therapeutic efficacy, several treatment groups were evaluated as follows. A similar overall experimental procedure was followed (Fig. 5A). Mice were fed with DSS

(2 wt % in water) for six consecutive days (days 1 to 6) to induce UC. The successful onset of UC was indicated by body weight loss on day 6 for all the DSS-induced groups (Fig. 5B). After that, Pt@PCN222-Mn-5, Pt NPs, or PCN222-Mn was administered by intraperitoneal injection to the mice on three consecutive days (days 7, 8, and 9). The therapeutic efficacy of the nanozymes was again evaluated by measuring the changes in body weight (Fig. 5C), colon lengths (Fig. 5, D and E), and levels of proinflammatory cytokines of TNF-α and IL-1β in colon tissues (Fig. 5, F and G) and by observing the histologically stained colon sections (Fig. 5H).

Results from this comparative analysis show that, as expected from the kinetic analysis, Pt@PCN222-Mn-5 showed a synergistic therapeutic effect. The therapeutic efficacy of Pt@PCN222-Mn-5 (1.0 mg/kg) was compared with a physical mixture of Pt (0.06 mg/kg) and PCN222-Mn (1.0 mg/kg). As shown in Fig. 5 (C to H), compared with the mice treated with the "Pt NPs + PCN222-Mn," the mice treated with Pt@PCN222-Mn-5 manifested less weight loss, longer colon length, lower levels of TNF-α and IL-1β, and better histological appearance. These results demonstrate that the observed kinetic synergies also extend to providing a synergistic therapeutic effect in vivo, an uncommon accomplishment in nanozyme-based therapies. We attribute this synergistic efficacy to the same nanoscale proximity effect exhibited in the kinetic analysis. This close proximity enhances the efficiency of the cascade reaction by confining the involved catalysts within a nanoscale space and removing diffusion barriers from the system (in the current case, the SOD- and CAT-like catalytic components were even integrated within a single Pt@PCN222-Mn-5 nanozyme) (*39*).

Last, we analyzed the dose-dependent efficacy of Pt@PCN222-Mn-5 and PCN222-Mn (0.1, 0.5, and 1.0 mg/kg). Unexpectedly, the treatment groups of both PCN222-Mn and Pt@PCN222-Mn-5 at 0.5-mg/kg nanozyme concentration had superior outcomes to the lower and higher concentrations. Figure 5 (B and C) shows that the group treated with Pt@PCN222-Mn-5 at 0.5 mg/kg even experienced body weight increases similar to the control group. Furthermore,
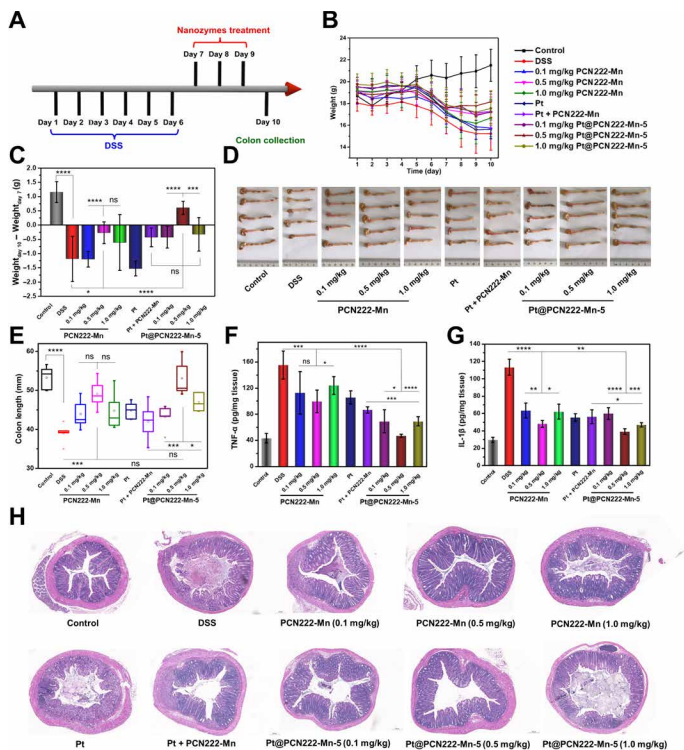
Fig. 5. UC therapy with Pt@PCN222-Mn-5. (**A**) Overall procedure of the animal experiment (DSS-induced colitis). (**B**) Daily body-weight development for 10 days. (**C**) Changes in body weight of mice before (day 7) and after indicated treatments (day 10). (**D**) Images of the colons and (**E**) the corresponding colon lengths in indicated groups. (**F**) IL-1β and (**G**) TNF-α levels in colon homogenates from indicated groups. (**H**) H&E-stained colonic sections of mice from indicated groups on day 10. The data are shown as means ± SD ($n = 5$). *$P < 0.05$, **$P < 0.01$, ***$P < 0.005$, and ****$P < 0.001$; ns, not significant; t test. Photo credit (D): Yufeng Liu, College of Engineering and Applied Sciences, Nanjing University.

Fig. 6. CD therapy with Pt@PCN222-Mn-5. (**A**) Overall procedure of the animal experiment [2,4,6-trinitro benzene sulfonic acid (TNBS)–induced colitis]. (**B**) Daily body-weight development after administering TNBS solution into the colon lumen. (**C**) Changes in body weight of mice before (day 9) and after indicated treatments (day 12). (**D**) Colon lengths and (**E**) the corresponding images of colons of indicated groups. The data are shown as means ± SD ($n = 5$). *$P < 0.05$, ***$P < 0.005$, and ****$P < 0.001$; ns, not significant; t test. Photo credit (E): Yuan Cheng, College of Engineering and Applied Sciences, Nanjing University.

colon lengths (Fig. 5, D and E), H&E-stained colonic tissue sections (Fig. 5H), colonic ROS levels (figs. S21 and S22), and colonic IL-1β and TNF-α levels (Fig. 5, F and G) of the Pt@PCN222-Mn-5 at the 0.5-mg/kg treatment group were nearly identical to those of the control group. No notable improvement in the therapeutic efficacy was observed between treatment groups given nanozyme concentrations of 0.1 and 1.0 mg/kg (Fig. 5, D to H). We attribute the lowered efficacy of the high-concentration group to the observed in vitro cytotoxicity at high dosage (fig. S16). These observations demonstrate that Pt@PCN222-Mn-5 is efficacious for the treatment of UC and that dosage must be tuned just as with traditional small-molecule therapies.

CD is another type of IBD. To explore the breadth of therapeutic applications of the Pt@PCN222-Mn-5 nanozyme, we additionally evaluated its efficacy as a therapy for CD (Fig. 6). The CD model was developed by using 2,4,6-trinitro benzene sulfonic acid (TNBS) to induce the disease state (*40*). Figure 6A summarizes the overall experimental procedure. Briefly, on day 1, mice were presensitized by absorption of TNBS solution through the skin. Seven days later, on day 8, mice were slowly administered TNBS solution into the colon lumen to induce CD. In addition to an untreated control group, a sham group was also used in which the TNBS solution was replaced with phosphate-buffered saline (PBS). The successful onset of CD was indicated by body weight loss on day 9 for all TNBS-treated
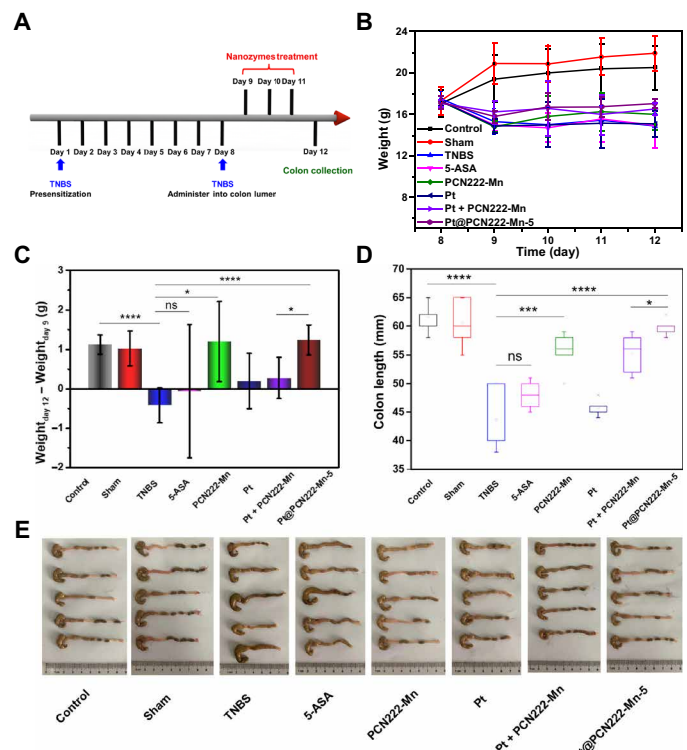
groups (Fig. 6B). Next, 5-ASA, PCN222-Mn, Pt, Pt physical mixed with PCN222-Mn, or Pt@PCN222-Mn-5 was administered by intraperitoneal injection to the mice on three consecutive days (days 9, 10, and 11). Comparison of body weight changes and colon lengths demonstrated the considerable therapeutic efficacy of the treatment groups of PCN222-Mn and Pt@PCN222-Mn at a concentration of 0.5 mg/kg (Fig. 6, C to E). By comparison, the group treated with 5-ASA at 0.5 mg/kg showed no obvious therapeutic effect on CD. Thus, we demonstrate that cascade nanozymes that directly alleviate disease chemistry have a potentially greater breadth and efficacy compared to traditional small-molecule medications in IBD treatment.

DISCUSSION
In summary, we have developed an integrated nanozyme with the ability to catalyze cascade reactions for ROS elimination. The integrated nanozyme not only has two spatially separated active sites, which can mimic SOD and CAT, but also has a confinement effect that enhances the overall reaction rate by increasing mass-transfer efficiency and reducing the transfer time between catalytic centers, as demonstrated by kinetic analysis. In vitro experiments showed that the cascade nanozyme has outstanding ROS-scavenging activity, excellent biocompatibility, and good aqueous dispersibility. We established an inflammatory animal model to evaluate the anti-ROS ability of the cascade nanozyme in vivo. To our delight, the

cascade nanozyme exhibited superior therapeutic efficacy toward both an UC and CD model state in mice, as compared to mice treated with an unintegrated mixture of the two nanozymes. Furthermore, in these animal models, we successfully achieved effective relief of both IBDs by optimizing the concentration of the cascade nanozyme. This work not only demonstrates that MOF-based nanozymes have excellent ROS-scavenging activities for in vivo inflammatory treatment but also provides a promising strategy to construct integrated nanozymes with multifunctional active sites for future applications.

MATERIALS AND METHODS
Reagents and materials
Commercially available reagents were of analytical grade and used without further purification. Methyl p-formylbenzoate and $ZrOCl_2 \cdot 8H_2O$ were purchased from Energy Chemical Co. Ltd. (Shanghai, China). Propionic acid was purchased from Shanghai Lingfeng Chemical Reagent Co. Ltd. (Shanghai, China). Pyrrole, PVP, DSS, hydroethidine (HE), 5-ASA, and PQ were purchased from Aladdin Chemical Co. Ltd. (Shanghai, China). H_2O_2, hydrochloric acid, and benzoic acid were purchased from Sinopharm Chemical Reagent Co. Ltd. (Shanghai, China). Chloroplatinic acid ($H_2PtCl_6 \cdot 6H_2O$), NBT, X, XO, and diethylene triamine pentaacetic acid (DTPA) were obtained from Sigma-Aldrich. 5,5-Dimethyl-1-pyrroline-N-oxide (DMPO) was obtained from Dojindo (Japan). DCFH-DA (2′,7′-dichlorofluorescin diacetate) was purchased from Beyotime Chemical Reagent Co. Ltd. (Jiangsu, China). All aqueous solutions were prepared with deionized water (18.2 megohm·cm, Millipore).

Instrumentation
^{1}H-NMR spectrum was obtained on a Bruker AM400 spectrometer, with tetramethylsilane as an internal standard. FTIR spectrum was recorded on a Thermo Nicolet Near FTIR Nexus 870 spectrometer. TEM imaging was performed on a Tecnai F20 microscope FEI (Field Electron and Iron Company) at an acceleration voltage of 200 kV. SEM images were collected on a Zeiss Ultra 55 microscope (Zeiss, Germany). PXRD patterns were measured with an ARL SCINTAC X'TRA diffractometer using Cu Kα radiation (Thermo Fisher Scientific). UV-visible absorption spectra were recorded on a UV-visible spectrophotometer with a 1-cm quartz cell (Purkinje General Instrument Co. Ltd., Beijing, China) and a microplate reader (SpectraMax M2e, Molecular Device Co. Ltd., Shanghai, China). Zeta potentials were measured on a Nanosizer ZS90 (Malvern). The amounts of Pt in Pt@PCN222-Mn-1, Pt@PCN222-Mn-3, and Pt@PCN222-Mn-5 were analyzed by an inductively coupled plasma atomic emission spectrometer (ICP-AES) (Avio 500, PerkinElmer). The quantitative fluorescence images of colons were recorded on a PerkinElmer In vivo Imaging System with an excitation wavelength of 465 nm and an emission wavelength of 520 nm. The generated oxygen (milligram per liter) was monitored by using a dissolved oxygen meter (SevenExcellence Multiparameter, Mettler Toledo Co. Ltd.).

Synthesis of TPP-COOMe and TCPP-Mn
TPP-COOMe [5,10,15,20-tetrakis(4-methoxycarbonylphenyl) porphyrin] was synthesized by following a previous procedure, with minor revisions (41). Methyl p-formylbenzoate (14 g) was dissolved in propionic acid (200 ml). Then, pyrrole (6 ml) was added dropwise in the solution. The mixed solution was refluxed for 12 hours

in darkness. After the reaction, the mixture was cooled to room temperature; the purple solid resultant was obtained by filtrating and washing with methanol and tetrahydrofuran (THF) for several times. ^{1}H-NMR (CDCl$_3$, 400 MHz): δ 8.81 (s, 8H), 8.44 (d, 8H), 8.29 (d, 8H), 4.11 (s, 12H), and 2.83 (s, 2H).

TCPP-Mn was synthesized as follows. TPP-COOMe (0.854 g) and MnCl$_2 \cdot 4H_2O$ (2.5 g) were dissolved in N,N')dimethylformamide (DMF; 100 ml). Then, the mixed solution was refluxed for 6 hours in darkness. After the solution was cooled to room temperature, H_2O (150 ml) was added and the solution was further stirred for 1 hour. The resultant precipitate was obtained by filtrating and washing with H_2O for three times. The obtained dark-greenish crystal was further dissolved in CHCl$_3$ and washed several times with H_2O. To obtain the TCPP-Mn, the as-synthesized dark-greenish crystal (0.75 g) was dissolved in MeOH (25 ml), THF (25 ml), and KOH solution (2.63 g of KOH in 25 ml of H_2O), and then the mixed solution was refluxed for 12 hours in darkness. THF and MeOH were removed by using a rotary evaporator, and then additional water and 1 M HCl were added to the solution to fully acidify the precipitate. The product of TCPP-Mn was obtained by filtration and then dried in vacuum. FTIR (KBr): ν = 3066, 2588, 1735, 1606, 1581, 1386, 1340, 1309, 1259, 1204, 1176, 1103, 1011, 865, 801, and 714 cm^{-1}.

Synthesis of nanoscale PCN222-Mn, Pt NPs, Pt@PCN222-Mn-1, Pt@PCN222-Mn-3, and Pt@PCN222-Mn-5
Nanoscale PCN222-Mn was synthesized according to a previous method, with minor modifications (42). TCPP-Mn (20 mg), $ZrOCl_2 \cdot 8H_2O$ (60 mg), and benzoic acid (580 mg) were dissolved in DMF (20 ml), and the mixture was magnetically stirred (300 rpm) at 90°C for 5 hours. After the solution was cooled to room temperature, PCN222-Mn NPs were obtained by centrifugation (15,000 rpm, 30 min) followed by washing with DMF for several times. The resulting PCN222-Mn was redispersed in DMF for storage.

Pt NPs were synthesized by following a previous procedure, with minor modifications (43). PVP (266 mg, M_w = 24,000) was dissolved in methanol (90 ml), and then H_2PtCl_6 (10 ml, 50 mM) was added to the solution. The mixture was refluxed for 3 hours under air. After that, methanol was removed by using a rotary evaporator, and then the NPs were precipitated by acetone for 3 hours and collected by centrifugation (6000 rpm, 5 min). The obtained Pt NPs were further purified with chloroform and hexane and then redispersed in DMF.

Nanoscale Pt@PCN222-Mn-1 was synthesized by dissolving TCPP-Mn (20 mg), $ZrOCl_2 \cdot 8H_2O$ (60 mg), and benzoic acid (580 mg) in 19 ml of DMF and 1 ml of as-synthesized PVP-Pt NPs (10 mM). The mixture was stirred (300 rpm) at 90°C for 5 hours. After the solution was cooled to room temperature, Pt@PCN222-Mn-1 NPs were obtained by centrifugation (15,000 rpm, 30 min) followed by washing with DMF for several times. The resulting Pt@PCN222-Mn-1 was redispersed in DMF for storage. Nanoscale Pt@PCN222-Mn-3 was synthesized by using the same protocol for Pt@PCN222-Mn-1, except that 17 ml of DMF and 3 ml of as-synthesized PVP-Pt NPs (10 mM) were used instead. Nanoscale Pt@PCN222-Mn-5 was synthesized by using the same protocol for Pt@PCN222-Mn-1, except that 15 ml of DMF and 5 ml of as-synthesized PVP-Pt NPs (10 mM) were used instead. The Pt contents in Pt@PCN222-Mn-1, Pt@PCN222-Mn-3, and Pt@PCN222-Mn-5 were quantified as 0.7, 2.2, and 6 wt %, respectively, by using ICP-AES.

Measurement of the SOD-like activity

HE, an $\cdot O_2^-$ fluorescence probe, was used to assess the amount of $\cdot O_2^-$. The SOD-like activity of TCPP, TCPP-Mn, and PCN222-Mn was evaluated by measuring the amount of $\cdot O_2^-$ with the HE probe. Typically, X (0.6 mM), XO (0.05 U/ml), and TCPP-Mn (40 μg/ml) were mixed in tris-HCl buffer (0.1 M, pH 7.52) at 37°C in 20 min. HE (0.5 mg/ml) was added to the solution for another 15-min reaction. Then, the fluorescence spectra were recorded, with excitation and emission wavelengths of 470 and 610 nm, respectively.

NBT, another $\cdot O_2^-$-sensitive probe, was used to evaluated the SOD-like activity of PCN222-Mn and Pt@PCN222-Mn. The detection method is shown in fig. S13 (A to D): Different concentrations of MOF-based nanozymes and NBT (0.05 mM) were mixed with X (0.15 mM) and XO (0.02 U/ml) in tris-HCl buffer (0.1 M, pH 7.52). The mixed solution samples were continuously monitored the absorbance at 550 nm in 5 min by using a microplate reader. The detection method is shown in Figs. 3 and 4: Different concentrations of nanozymes were mixed with X (0.6 mM) and XO (0.05 U/ml) in tris-HCl buffer (0.1 M, pH 7.52) at 37°C for 5 min. Then, NBT (100 μg/ml) was added to the mixed solution to continuously monitor the absorbance at 550 nm in 5 min by using a microplate reader.

Measurement of the CAT-like activity

The CAT-like activity of nanozymes was evaluated by monitoring the generated oxygen from the decomposition of H_2O_2. Typically, different concentrations of nanozymes were mixed with H_2O_2 in 5.0 ml of tris-HCl buffer (0.1 M, pH 7.52). The oxygen solubility (milligram per liter) was monitored in 5 min by using a dissolved-oxygen meter.

Measurement of EPR

EPR spectra were recorded on a Bruker A300 spectrometer (X-band) at room temperature, with a frequency of 9.835 GHz, a microwave power of 4.97 mW, and a modulation amplitude of 1.0 G. The sample had a final concentration of X (0.5 mM) and XO (0.22 mU), Pt@PCN222-Mn (0.044 mg/ml), PCN222-Mn (0.044 mg/ml), Pt NPs (3.33 μg/ml), PCN222-Mn (0.044 mg/ml) + Pt (3.33 μg/ml), and DMPO (22.5 mg/ml) in 100 mM potassium phosphate buffer that contained 25 μM DTPA (pH 7.4).

Cytotoxicity assay

CT-26 cells were refreshed in high-glucose Dulbecco's modified Eagle's medium (DMEM) culture medium containing 5% fetal bovine serum and 1% penicillin-streptomycin (10,000 U/ml) under the atmosphere of 5% CO_2 at 37°C. CT-26 cells with a density of 8×10^3 per well were cultured in 96-well plates for 24 hours at 37°C. Then, nanozymes at different concentrations (10, 20, 40, 80, 100, 150, and 200 μg/ml) were correspondingly added into the 96-well plates for another 24 hours. Cell viability was tested by using the CCK-8 assay.

Intracellular ROS-scavenging detection

The intracellular level of ROS was monitored by using the fluorescent probe of DCFH-DA with the excitation and emission wavelengths at 488 and 525 nm, respectively. CT-26 cells with a density of 8×10^3 per well were cultured in 96-well plates for 24 hours at 37°C. Then, nanozymes at different concentrations (0.1, 0.5, and 1.0 μg/ml) were separately added into the 96-well plates for another 24 hours. The cells were then washed by PBS (pH 7.4) in triplicate. Subsequently, DCFH-DA (0.01 mM) in DMEM was added into the 96-well plates

for culturing 30 min. After 30 min, the medium was refreshed three times, and then PQ with a concentration of 5 mM was added for 4 hours incubation to produce intracellular ROS.

In vivo anti-inflammation

All the animal studies were approved by the Committee for Experimental Animals Welfare and Ethics of Nanjing Drum Tower Hospital, the Affiliated Hospital of Nanjing University Medical School. The UC model of mice was chosen and established to evaluate the anti-inflammation of the nanozymes. Male C57BL/6 mice (18 to 20 g) were acclimatized for 7 days and randomly divided into various groups with five mice per group. We replaced the drinking water of each group with 2 wt % DSS–containing sterile water, leaving one group as control, and this day was designated as day 1. The mice with DSS-induced colitis were aseptically and intraperitoneally injected with different concentrations of PCN222-Mn and Pt@PCN222-Mn-5 in three consecutive days (days 7, 8, and 9). The mice of all groups were sacrificed after being anesthetized with diethyl ether on day 10. The length of whole colon was recorded.

The TNBS colitis model of mice was chosen and established to evaluate the anti-inflammation of nanozymes. Male C57BL/6 mice (18 to 20 g) were acclimatized for 7 days and randomly divided into various groups with five mice per group. The TNBS-induced mice were presensitized with 1 wt % TNBS and kept for 7 days and treated with 2.5 wt % TNBS enema on day 8. Nanozymes and 5-ASA were treated in the same protocol as the DSS model described above.

Pathological evaluation

The colons from all groups were fixed with 10% formalin, processed routinely, dried and embedded into paraffin, sectioned at a thickness of 4 mm, and stained with H&E. The stained tissues were examined and photographed by using an optical microscopy.

Cytokines determination with ELISA kit

For proinflammatory cytokines evaluation, the amount of TNF-α and IL-1β in colon homogenate was quantified by an enzyme-linked immunosorbent assay (ELISA) test. The colon tissue with the length of about 5 mm from each mouse was weighed and homogenated in 1.5 ml of saline at 4°C. The resultant homogenate was centrifuged at 2000 rpm for 20 min at 4°C, and the supernatant was collected for evaluation. Commercial mouse IL-1β and TNF-α ELISA Kits (Neobioscience Technology Co, Ltd, China) were used to quantify the amounts of IL-1β and TNF-α in the homogenate of colon tissues.

Immunohistochemical staining and average analysis of IHC images

IL-1β and TNF-α IHC staining was carried out on formalin-fixed sections with a thickness of 2 μm. The sections were incubated with 0.3 volume % hydrogen peroxide containing methanol for 10 min, washed with deionized water for three times, and boiled in 0.01 M citrate buffer (pH 6.0) at 90°C for 10 min of antigen retrieval. The obtained samples were then incubated with primary antibodies of anti–IL-1β and anti–TNF-α, respectively, at 4°C overnight, and with secondary horseradish peroxidase–labeled antibody for 1 hour at 37°C, following chromogenizing with diaminobenzidine and nuclear staining with hematoxylin. The stained tissues were examined and photographed by using an optical microscopy. The analysis of brownish staining in six different areas of each tissue sample was performed with ImageJ software, and average results were calculated

by a scoring equation that is often used for IHC analysis (score = 4× high positive + 3× positive + 2× low positive + negative).

Ex vivo ROS evaluation

The UC model of mice of four groups with five mice per group was established again following the same protocol for ex vivo ROS evaluation. The ROS-scavenging efficacy of both nanozymes with the dose of 0.5 mg/kg was evaluated by 0.5 hour after intraperitoneal injection of DCFH-DA (0.7 mg per mouse) on day 10. The fluorescence images of the whole colons from all groups were recorded by using a PerkinElmer In vivo Imaging System with an excitation wavelength of 465 nm and an emission wavelength of 520 nm.

In vivo toxicity toward live tissues

In vivo toxicity of the nanozymes toward main organs was evaluated by pathological observation of the tissues, including heart, liver, spleen, lung, and kidney 7 days after intraperitoneal injection of PCN222-Mn and Pt@PCN222-Mn-5 with the dose of 1.0 mg/kg, respectively, from the groups of reestablished model. These tissues were collected and rinsed with deionized water and fixed in 10% neutral buffered formalin. The tissues were processed routinely, dried and embedded into paraffin, sectioned at a thickness of 4 mm, stained with H&E, and examined and photographed by using an optical microscopy.

SUPPLEMENTARY MATERIALS

Supplementary material for this article is available at http://advances.sciencemag.org/cgi/content/full/6/29/eabb2695/DC1

View/request a protocol for this paper from *Bio-protocol*.

REFERENCES AND NOTES

1. E. Yeger-Lotem, S. Sattath, N. Kashtan, S. Itzkovitz, R. Milo, R. Y. Pinter, U. Alon, H. Margalit, Network motifs in integrated cellular networks of transcription-regulation and protein-protein interaction. *Proc. Natl. Acad. Sci. U.S.A.* **101**, 5934–5939 (2004).

2. K. S. Rabe, J. Müller, M. Skoupi, C. M. Niemeyer, Cascades in compartments: En route to machine-assisted biotechnology. *Angew. Chem. Int. Ed.* **56**, 13574–13589 (2017).

3. G. Sachdeva, A. Garg, D. Godding, J. C. Way, P. A. Silver, In vivo co-localization of enzymes on RNA scaffolds increases metabolic production in a geometrically dependent manner. *Nucleic Acids Res.* **42**, 9493–9503 (2014).

4. X. Lian, A. Erazo-Oliveras, J.-P. Pellois, H.-C. Zhou, High efficiency and long-term intracellular activity of an enzymatic nanofactory based on metal-organic frameworks. *Nat. Commun.* **8**, 2075 (2017).

5. W.-H. Chen, M. Vázquez-González, A. Zoabi, R. Abu-Reziq, I. Willner, Biocatalytic cascades driven by enzymes encapsulated in metal-organic framework nanoparticles. *Nat. Catal.* **1**, 689–695 (2018).

6. Y. Liu, J. Du, M. Yan, M. Y. Lau, J. Hu, H. Han, O. O. Yang, S. Liang, W. Wei, H. Wang, J. Li, X. Zhu, L. Shi, W. Chen, C. Ji, Y. Lu, Biomimetic enzyme nanocomplexes and their use as antidotes and preventive measures for alcohol intoxication. *Nat. Nanotechnol.* **8**, 187–192 (2013).

7. L. Gao, J. Zhuang, L. Nie, J. Zhang, Y. Zhang, N. Gu, T. Wang, J. Feng, D. Yang, S. Perrett, X. Yan, Intrinsic peroxidase-like activity of ferromagnetic nanoparticles. *Nat. Nanotechnol.* **2**, 577–583 (2007).

8. H. Wei, E. Wang, Nanomaterials with enzyme-like characteristics (nanozymes): Next-generation artificial enzymes. *Chem. Soc. Rev.* **42**, 6060–6093 (2013).

9. J. Wu, X. Wang, Q. Wang, Z. Lou, S. Li, Y. Zhu, L. Qin, H. Wei, Nanomaterials with enzyme-like characteristics (nanozymes): Next-generation artificial enzymes (II). *Chem. Soc. Rev.* **48**, 1004–1076 (2019).

10. D. Jiang, D. Ni, Z. T. Rosenkrans, P. Huang, X. Yan, W. Cai, Nanozyme: New horizons for responsive biomedical applications. *Chem. Soc. Rev.* **48**, 3683–3704 (2019).

11. Y. Huang, J. Ren, X. Qu, Nanozymes: Classification, catalytic mechanisms, activity regulation, and applications. *Chem. Rev.* **119**, 4357–4412 (2019).

12. L. Huang, J. Chen, L. Gan, J. Wang, S. Dong, Single-atom nanozymes. *Sci. Adv.* **5**, eaav5490 (2019).

13. G. Y. Tonga, Y. Jeong, B. Duncan, T. Mizuhara, R. Mout, R. Das, S. T. Kim, Y.-C. Yeh, B. Yan, S. Hou, V. M. Rotello, Supramolecular regulation of bioorthogonal catalysis in cells using nanoparticle-embedded transition metal catalysts. *Nat. Chem.* **7**, 597–603 (2015).

14. F. Manea, F. B. Houillon, L. Pasquato, P. Scrimin, Nanozymes: Gold-nanoparticle-based transphosphorylation catalysts. *Angew. Chem. Int. Ed.* **43**, 6165–6169 (2004).

15. Z. Zhang, X. Zhang, B. Liu, J. Liu, Molecular imprinting on inorganic nanozymes for hundred-fold enzyme specificity. *J. Am. Chem. Soc.* **139**, 5412–5419 (2017).

16. M. Soh, D.-W. Kang, H.-G. Jeong, D. Kim, D. Y. Kim, W. Yang, C. Song, S. Baik, I.-Y. Choi, S.-K. Ki, H. J. Kwon, T. Kim, C. K. Kim, S.-H. Lee, T. Hyeon, Ceria-Zirconia nanoparticles as an enhanced multi-antioxidant for sepsis treatment. *Angew. Chem. Int. Ed.* **56**, 11399–11403 (2017).

17. C. N. Loynachan, A. P. Soleimany, J. S. Dudani, Y. Lin, A. Najer, A. Bekdemir, Q. Chen, S. N. Bhatia, M. M. Stevens, Renal clearable catalytic gold nanoclusters for in vivo disease monitoring. *Nat. Nanotechnol.* **14**, 883–890 (2019).

18. W. Zhang, S. Hu, J.-J. Yin, W. He, W. Lu, M. Ma, N. Gu, Y. Zhang, Prussian blue nanoparticles as multienzyme mimetics and reactive oxygen species scavengers. *J. Am. Chem. Soc.* **138**, 5860–5865 (2016).

19. M. A. Komkova, E. E. Karyakina, A. A. Karyakin, Catalytically synthesized Prussian blue nanoparticles defeating natural enzyme peroxidase. *J. Am. Chem. Soc.* **140**, 11302–11307 (2018).

20. Z. Xi, X. Cheng, Z. Gao, M. Wang, T. Cai, M. Muzzio, E. Davidson, O. Chen, Y. Jung, S. Sun, Y. Xu, X. Xia, Strain effect in palladium nanostructures as nanozymes. *Nano Lett.* **20**, 272–277 (2020).

21. H. Cheng, L. Zhang, J. He, W. Guo, Z. Zhou, X. Zhang, S. Nie, H. Wei, Integrated nanozymes with nanoscale proximity for in vivo neurochemical monitoring in living brains. *Anal. Chem.* **88**, 5489–5497 (2016).

22. Y. Hu, H. Cheng, X. Zhao, J. Wu, F. Muhammad, S. Lin, J. He, L. Zhou, C. Zhang, Y. Deng, P. Wang, Z. Zhou, S. Nie, H. Wei, Surface-enhanced raman scattering active gold nanoparticles with enzyme-mimicking activities for measuring glucose and lactate in living tissues. *ACS Nano* **11**, 5558–5566 (2017).

23. M. Huo, L. Wang, Y. Chen, J. Shi, Tumor-selective catalytic nanomedicine by nanocatalyst delivery. *Nat. Commun.* **8**, 357 (2017).

24. P. B. O'Mara, P. Wilde, T. M. Benedetti, C. Andronescu, S. Cheong, J. J. Gooding, R. D. Tilley, W. Schuhmann, Cascade reactions in nanozymes: Spatially separated active sites inside Ag-Core–Porous-Cu-shell nanoparticles for multistep carbon dioxide reduction to higher organic molecules. *J. Am. Chem. Soc.* **141**, 14093–14097 (2019).

25. P. Zhang, D. Sun, A. Cho, S. Weon, S. Lee, J. Lee, J. W. Han, D.-P. Kim, W. Choi, Modified carbon nitride nanozyme as bifunctional glucose oxidase-peroxidase for metal-free bioinspired cascade photocatalysis. *Nat. Commun.* **10**, 940 (2019).

26. Y. Zhao, Y. Huang, H. Zhu, Q. Zhu, Y. Xia, Three-in-one: Sensing, self-assembly, and cascade catalysis of cyclodextrin modified gold nanoparticles. *J. Am. Chem. Soc.* **138**, 16645–16654 (2016).

27. X. Hu, F. Li, F. Xia, X. Guo, N. Wang, L. Liang, B. Yang, K. Fan, X. Yan, D. Ling, Biodegradation-mediated enzymatic activity-tunable molybdenum oxide nanourchins for tumor-specific cascade catalytic therapy. *J. Am. Chem. Soc.* **142**, 1636–1644 (2020).

28. M. Mittal, M. R. Siddiqui, K. Tran, S. P. Reddy, A. B. Malik, Reactive oxygen species in inflammation and tissue injury. *Antioxid. Redox Signal.* **20**, 1126–1167 (2014).

29. J. S. Wright, E. R. Johnson, G. A. DiLabio, Predicting the activity of phenolic antioxidants: Theoretical method, analysis of substituent effects, and application to major families of antioxidants. *J. Am. Chem. Soc.* **123**, 1173–1183 (2001).

30. T. Fukai, M. Ushio-Fukai, Superoxide dismutases: Role in redox signaling, vascular function, and diseases. *Antioxid. Redox Signal.* **15**, 1583–1606 (2011).

31. C. J. Weydert, J. J. Cullen, Measurement of superoxide dismutase, catalase and glutathione peroxidase in cultured cells and tissue. *Nat. Protoc.* **5**, 51–66 (2010).

32. J. Yao, Y. Cheng, M. Zhou, S. Zhao, S. Lin, X. Wang, J. Wu, S. Li, H. Wei, ROS scavenging Mn$_3$O$_4$ nanozymes for in vivo anti-inflammation. *Chem. Sci.* **9**, 2927–2933 (2018).

33. J. Zhao, W. Gao, X. Cai, J. Xu, D. Zou, Z. Li, B. Hu, Y. Zheng, Nanozyme-mediated catalytic nanotherapy for inflammatory bowel disease. *Theranostics* **9**, 2843–2855 (2019).

34. Z. Wang, Y. Zhang, E. Ju, Z. Liu, F. Cao, Z. Chen, J. Ren, X. Qu, Biomimetic nanoflowers by self-assembly of nanozymes to induce intracellular oxidative damage against hypoxic tumors. *Nat. Commun.* **9**, 3334 (2018).

35. D. Feng, Z.-Y. Gu, J.-R. Li, H.-L. Jiang, Z. Wei, H.-C. Zhou, Zirconium-metalloporphyrin PCN-222: Mesoporous metal-organic frameworks with ultrahigh stability as biomimetic catalysts. *Angew. Chem. Int. Ed.* **51**, 10307–10310 (2012).

36. G. Lu, S. Li, Z. Guo, O. K. Farha, B. G. Hauser, X. Qi, Y. Wang, X. Wang, S. Han, X. Liu, J. S. DuChene, H. Zhang, Q. Zhang, X. Chen, J. Ma, S. C. J. Loo, W. D. Wei, Y. Yang, J. T. Hupp, F. Huo, Imparting functionality to a metal-organic framework material by controlled nanoparticle encapsulation. *Nat. Chem.* **4**, 310–316 (2012).

37. G. Li, S. Zhao, Y. Zhang, Z. Tang, Metal-organic frameworks encapsulating active nanoparticles as emerging composites for catalysis: Recent progress and perspectives. *Adv. Mater.* **30**, 1800702 (2018).

38. K. A. Head, J. S. Jurenka, Inflammatory bowel disease Part 1: Ulcerative colitis—Pathophysiology and conventional and alternative treatment options. *Altern. Med. Rev.* **8**, 247–283 (2003).

39. Q. Yang, Q. Xu, H.-L. Jiang, Metal-organic frameworks meet metal nanoparticles: Synergistic effect for enhanced catalysis. *Chem. Soc. Rev.* **46**, 4774–4808 (2017).

40. S. Wirtz, C. Neufert, B. Weigmann, M. F. Neurath, Chemically induced mouse models of intestinal inflammation. *Nat. Protoc.* **2**, 541–546 (2007).

41. D. Feng, W.-C. Chung, Z. Wei, Z.-Y. Gu, H.-L. Jiang, Y.-P. Chen, D. J. Darensbourg, H.-C. Zhou, Construction of ultrastable porphyrin Zr metal-organic frameworks through linker elimination. *J. Am. Chem. Soc.* **135**, 17105–17110 (2013).

42. J. Park, Q. Jiang, D. Feng, L. Mao, H.-C. Zhou, Size-controlled synthesis of porphyrinic metal-organic framework and functionalization for targeted photodynamic therapy. *J. Am. Chem. Soc.* **138**, 3518–3525 (2016).

43. T. Teranishi, M. Hosoe, T. Tanaka, M. Miyake, Size control of monodispersed Pt nanoparticles and their 2D organization by electrophoretic deposition. *J. Phys. Chem. B* **103**, 3818–3827 (1999).